Atomically Precise $Au_{24}Pt(thiolate)_{12}(ditholate)_3$ Nanoclusters with Excellent Electrocatalytic Hydrogen Evolution Reactivity

Miyu Sera,[1] Sakiat Hossain,*[2] Sara Yoshikawa,[1] Kana Takemae,[1] Ayaka Ikeda,[1] Tomoya Tanaka,[1] Taiga Kosaka,[1] Yoshiki Niihori,[2] Tokuhisa Kawawaki[1,2] and Yuichi Negishi*[2,3]

[1]Department of Applied Chemistry, Faculty of Science, Tokyo University of Science, Kagurazaka, Shinjuku-ku, Tokyo 162−8601, Japan

[2]Research Institute for Science & Technology, Tokyo University of Science, Kagurazaka, Shinjuku-ku, Tokyo 162−8601, Japan

[3]Institute of Multidisciplinary Research for Advanced Materials, Tohoku University, Katahira, Aoba-ku, Sendai 980−8577, Japan

KEYWORDS Dithiolate ligand; Au–Pt alloy nanocluster; Geometric and electronic structure; Hydrogen evolution reaction; Proton-accessible nanocluster surface area

ABSTRACT: $[Au_{24}Pt(C6)_{18}]^0$ (C6 = 1-hexanethiolate) is twice as active as commercial Pt nanoparticles in promoting the electrocatalytic hydrogen evolution reaction (HER), thereby attracting attention as new HER catalysts with well-controlled geometric structures. In this study, we succeeded in synthesizing two new Au–Pt alloy nanoclusters, namely $[Au_{24}Pt(TBBT)_{12}(TDT)_3]^0$ (TBBT = 4-*tert*-butylbenzenethiolate; TDT = thiodithiolate) and $[Au_{24}Pt(TBBT)_{12}(PDT)_3]^0$ (PDT = 1,3-propanedithiolate), by exchanging all the ligands of $[Au_{24}Pt(PET)_{18}]^0$ (PET = 2-phenylethanethiolate) with mono- or dithiolates. Although $[Au_{24}Pt(TBBT)_{12}(TDT)_3]^0$ was synthesized serendipitously, a similar cluster, $[Au_{24}Pt(TBBT)_{12}(PDT)_3]^0$, was subsequently obtained by selecting the appropriate reaction conditions and optimal combination of thiolate and dithiolate ligands. Single crystal X-ray diffraction analyses revealed that the lengths and orientations of –Au(I)–SR–Au(I)– staples in $[Au_{24}Pt(TBBT)_{12}(TDT)_3]^0$ and $[Au_{24}Pt(TBBT)_{12}(PDT)_3]^0$ were different from those in $[Au_{24}Pt(C6)_{18}]^0$, $[Au_{24}Pt(PET)_{18}]^0$, and $[Au_{24}Pt(TBBT)_{18}]^0$, and these subtle differences were reflected in the geometric and electronic structures as well as the HER activities of $[Au_{24}Pt(TBBT)_{12}(TDT)_3]^0$ and $[Au_{24}Pt(TBBT)_{12}(PDT)_3]^0$. Accordingly, the HER activities of products $[Au_{24}Pt(TBBT)_{12}(TDT)_3]^0$ and $[Au_{24}Pt(TBBT)_{12}(PDT)_3]^0$ were, respectively, 3.5 and 4.9 times higher than those of $[Au_{24}Pt(C6)_{18}]^0$ and $[Au_{24}Pt(TBBT)_{18}]^0$.

1. INTRODUCTION

Hydrogen (H_2) has a high mass-based energy density[1] and produces only water (H_2O) as a combustion byproduct in a fuel cell engine. On this basis, H_2 is considered one of the most important fuels in any future "net zero carbon" society. At present, natural gas reforming/gasification is widely used to produce H_2 because it is the most efficient and least expensive approach. However, this process is neither cost effective nor environmentally friendly.[2,3] As an alternative, pure H_2 (also referred to as green H_2) can be obtained from H_2O via electrocatalytic techniques. However, the most efficient and durable electrocatalysts currently available for promoting the hydrogen evolution reaction (HER) are nanoparticles (NPs) made from expensive rare metals, such as platinum (Pt),[4,5] which prevents the widespread adoption of H_2 as an affordable fuel. To shift to a "net zero carbon" society, it is indispensable to produce more appropriate catalysts with a higher activity than Pt NP-based catalysts.

Recently, Lee et al. reported that a catalyst comprising $Au_{24}Pt$ nanoclusters (NCs) protected by 1-hexanethiolates (C6), $[Au_{24}Pt(C6)_{18}]^0$ (Figure **S1a**), exhibits twice the activity of a model Pt catalyst comprising 20 wt% Pt on Vulcan carbon black (CB).[6] Unlike NPs, atomically precise noble metal NCs[7] protected by thiolates (SR; $M_m(SR)_n$, where m = the number of metal atoms and n = the number of thiolates) tend to have unique but uniform geometric and electronic structures.[8–14] Consequently, the characteristics of SR-protected monodisperse NCs are readily correlated with their geometric structures.[15–24] As an example, Our group previously studied the electrocatalytic properties of $[Au_{25}(PET)_{18}]^0$ (PET = 2-phenylethanethiolate; Figure **S1b**), $[Au_{38}(PET)_{24}]^0$, $[Au_{130}(PET)_{50}]^0$, $[Au_{144}(PET)_{60}]^0$, $[Au_{329}(PET)_{84}]^0$, $[Au_{25}(C6)_{18}]^0$, $[Au_{25}(C12)_{18}]^0$ (C12 = 1-dodecanethiolate; Figure **S1c**), $[Au_{20.5}Ag_{4.5}(PET)_{18}]^0$, $[Au_{23.7}Cu_{1.3}(PET)_{18}]^0$, $[Au_{24}Pd(PET)_{18}]^0$, and $[Au_{25}(PET)_{18}]^-$ NCs and revealed the relationships between chemical composition and HER activity.[25] In addition, owing to the high HER activity of $[Au_{24}Pt(C6)_{18}]^0$, we recently produced new Au–Pt alloy NCs from $[Au_{24}Pt(PET)_{18}]^0$ (**1**; Table **1**) using a ligand exchange method. The new NC, $[Au_{24}Pt(TBBT)_{18}]^0$ (TBBT = 4-*tert*-butylbenzenethiolate; Figure **S1d**; **2**; Table **1**),[26,27] were synthesized by controlling the reaction temperature, reaction time, and TBBTH (4-*tert*-butylbenzenethiol) concentration. However, the HER activity of this new material is similar to those previously reported for $[Au_{24}Pt(C6)_{18}]^0$. This outcome is attributed to the similar $Au_{24}PtS_{18}$ frame structures of the catalysts and the similar length of the ligands (C6 and TBBT). These ligands stabilize $Au_{24}Pt$ NCs but restrict the access of protons (H^+) to the $Au_{12}Pt$ metal cores serving as the active sites for the HER. To improve the HER activity of SR-protected $Au_{24}Pt$ NCs, the access of H^+ to the $Au_{12}Pt$ core has to be increased by tuning the structure.

Table 1. Chemical Formula and Molecular Weight of 1−4 and 2'−3'

No.	chemical formula	exp. vs calc.	molecular weight
1	$[Au_{24}Pt(PET)_{18}]^0$	exp.	7391.93
2	$[Au_{24}Pt(TBBT)_{18}]^0$	exp.	7896.49
3	$[Au_{24}Pt(TBBT)_{12}(TDT)_3]^0$	exp.	7277.89
4	$[Au_{24}Pt(TBBT)_{12}(PDT)_3]^0$	exp.	7224.02
2'	$[Au_{24}Pt(C1)_{18}]^0$	calc.	5769.08
3'	$[Au_{24}Pt(C1)_{12}(TDT)_3]^0$	calc.	5858.95
4'	$[Au_{24}Pt(C1)_{12}(PDT)_3]^0$	calc.	5805.08

Herein, we report the synthesis of two new Au–Pt alloy NCs, namely $[Au_{24}Pt(TBBT)_{12}(TDT)_3]^0$ (**3**; Table **1**) and $[Au_{24}Pt(TBBT)_{12}(PDT)_3]^0$ (**4**; Table **1**) (TDT = thiodithiolate and PDT = 1,3-propanedithiolate; Figure **S1e,f**). These NCs contain thiolate (TBBT) and dithiolate (TDT or PDT) ligands (Scheme **1**).[28,29] The geometric and electronic structures of these NCs were evaluated using single crystal X-ray diffraction (SCXRD), ultraviolet-visible (UV-vis)-near infrared (NIR) spectroscopy, and density functional theory (DFT) calculations. Detailed analyses of the SCXRD patterns of **3** and **4** and the data previously reported for **2** established that the surface staple structures and orientations of **3** and **4** were significantly different from those of **2** (Scheme **1**), despite their similar icosahedral $Au_{12}Pt$ cores, resulting in the exposure of the gold (Au) atoms of the metal core on the outside. These differences were also evident in the absorption spectra, redox potentials, and energy gaps associated with the highest occupied molecular orbitals (HOMOs) and lowest unoccupied molecular orbitals (LUMOs). These modified surface staple structures prompted an exploration of the electrocatalytic properties of the new NCs. Electrochemical HER experiments revealed that both **3** and **4** functioned as electrocatalysts, and the mass-based activities of **3** and **4** were, respectively, 3.5 and 4.9 times that of other $Au_{24}Pt(SR)_{18}$ NCs, such as $[Au_{24}Pt(C6)_{18}]^0$ and **2**.

2. RESULTS AND DISCUSSION

2.1. Synthesis and Characterization

Precursor NC **1** was synthesized following a reported method (Scheme **S1**).[30] Subsequently, **2** was prepared by completely exchanging all 18 PET ligands of **1** with TBBT at 60 °C using a modified version of the method for synthesizing **2**, which was previously reported by the authors[26] (Scheme **S2**). During this high-temperature ligand exchange reaction, greenish-brown product was generated and isolated by preparative thin-layer chromatography (PTLC). The purity and composition of the isolated product were confirmed by comparing the UV-vis spectroscopy and electrospray ionization-mass spectrometry (ESI-MS) data of the product with the data reported for $[Au_{24}Pt(TBBT)_{18}]^0$ (Figure **S2**).[26]

Interestingly, **3** was serendipitously obtained while attempting to synthesize **2** using 97% pure TBBTH (TCI Chemicals) (Schemes **1** and **S3**). A blackish-green crude reaction mixture was obtained following the exchange reaction, and its UV-vis absorption spectrum was notably different from that expected for **2** (Figure **1a**). Major product **3** was separated by PTLC (Figure **S3**), and its purity was verified by reverse-phase high-performance liquid chromatography (RP-HPLC) (Figure **1b**). The separated product generated only one RP-HPLC peak, confirming that it was pure. However, the retention time (30.9 min) of this peak was different from that of **2** (31.7 min), further indicating that a new NC was obtained.

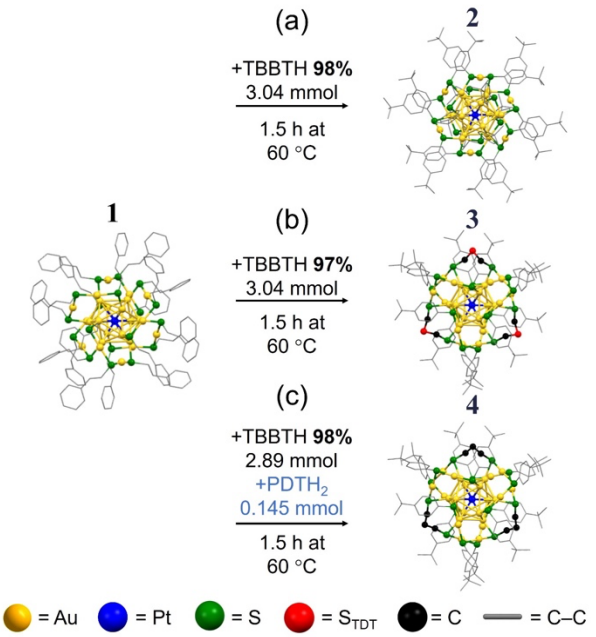

Scheme 1. Schematic of the synthesis of (a) **2**, (b) **3**, and (c) **4** from **1**.

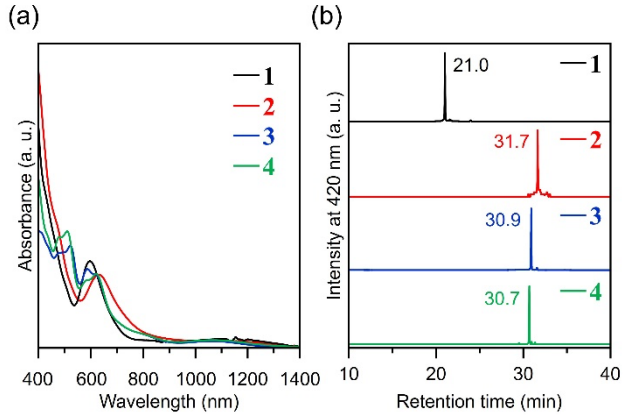

Figure 1. (a) UV-vis spectra and (b) RP-HPLC chromatograms of **1**−**4**.

Efforts to determine the chemical composition of the newly formed NC using ESI-MS (Figure **S4**) proved unsuccessful[31] because the major peak (single peak) could not be assigned to any feasible chemical composition based on various combinations of the initial (PET) and exchanging (TBBT) ligands or their fragments, such as S^{2-},[32] with Au and Pt from precursor **1** (Table **S1**). To determine whether newly formed **3** contained any of the initial thiolate, namely PET from **1** ($[Au_{24}Pt(PET)_{18}]^0$), a different starting NC, $[Au_{24}Pt(C6)_{18}]^0$, was used to synthesize **3** (Scheme **S4**). Surprisingly, the newly formed NC exhibited the same ESI-MS and UV-vis spectra as the material generated using **1** (Figure **S5**), confirming that the same NCs were formed in both reactions. Hence, the new NCs did not contain the starting thiolate (PET or C6) but instead

incorporated either a new ligand generated in situ or impurities present in TBBTH.

Although the composition of the newly formed NC could not be identified, the single peak observed in the RP-HPLC (Figure **1b**) and ESI-MS data (Figure **S4**) prompted an attempt to crystallize the obtained NC. A rod-shaped single crystal was eventually grown from a mixture of dichloromethane and ethanol (Figure **S6**) after multiple attempts using various crystallization methods and solvent combinations. SCXRD analysis revealed that the chemical composition of the new NC was $[Au_{24}Pt(TBBT)_{12}(TDT)_3]^0$ (Table **1**), which agreed with the peak positions and isotopic pattern of the ESI-MS spectrum (Figure **S5**).

Interestingly, when the same reaction conditions were employed with 98% pure TBBTH (FUJIFILM Wako Pure Chemical Corporation) as the exchanging ligand (Scheme **S2**), **2** was produced instead of **3**. This finding indicated that $HSCH_2SCH_2SH$ ($TDTH_2$) was present as an impurity in 97% TBBTH.[33]

To provide further evidence, we conducted a thiolate-exchange reaction of **1** using a mixture of two commercially available thiols, 98% pure TBBTH and 1,3-propanedithiol ($PDTH_2$) (Schemes **1c** and **S5**), a structural homologue of $TDTH_2$. The UV-vis spectrum of the crude reaction mixture was similar to that of **3**, suggesting that a structural homologue of **3** was obtained. Subsequent purification of the main product via PTLC (Figure **S7**), followed by an ESI-MS analysis (Figure **S8**), confirmed that this material comprised $[Au_{24}Pt(TBBT)_{12}(PDT)_3]^0$ (**4**; Table **1**).

2.2. Electronic Structures

2.2.1 UV-vis-NIR Spectroscopy. The UV-vis-NIR absorption spectrum of product **3** was markedly different from that of **2**, which contained a strong peak with a maximum at 632 nm, a broad shapeless peak below 500 nm, and a less intense peak in the NIR region with a maximum at 1125 nm (Figure **1a** and **S9Aa**). The peak at 632 nm was asymmetrically split into two peaks with broad maxima at 590 and 620 nm (Figure **1a** and **S9Ab**). In addition, **3** provided a pair of new, partially overlapped asymmetrical peaks with broad maxima at 475 and 523 nm. Interestingly, there were no significant changes in the shape or position of the peak in the NIR region, indicating that the structural difference, from **2** to **3**, did not greatly affect the absorption properties of icosahedral $Au_{12}Pt$.[34] The UV-vis-NIR spectrum of **4** was also similar to that of **3** (Figure **1a** and **S9Ac**). However, peaks in the range of 570–680 nm showed an opposite trend. Specifically, **4** provided a more intense absorption peak at approximately 620 nm, whereas **3** generated a higher absorption peak at approximately 590 nm.

2.2.2. DFT Calculations. Both DFT and time-dependent (TD)-DFT calculations using the Gaussian program were employed to elucidate the electronic structures of these products. In these calculations, the structures of **2**–**4** obtained from SCXRD data (see Sec. 2.3) were used as the initial models, while TBBT was modeled using methanethiolate (C1) to reduce the calculation cost (Figure **S10**). No changes were made to the TDT moiety of **3** nor PDT moiety of **4** (Figure **S10**). Figures **2** and **S11** presents the predicted orbitals and simulated absorption spectra of $[Au_{24}Pt(C1)_{18}]^0$ (**2'**), $[Au_{24}Pt(C1)_{12}(TDT)_3]^0$ (**3'**), and $[Au_{24}Pt(C1)_{12}(PDT)_3]^0$ (**4'**) (Table **1**). Consistent with the experimental spectra (Figure **S9B**), the absorption intensity increased as the energy increased.

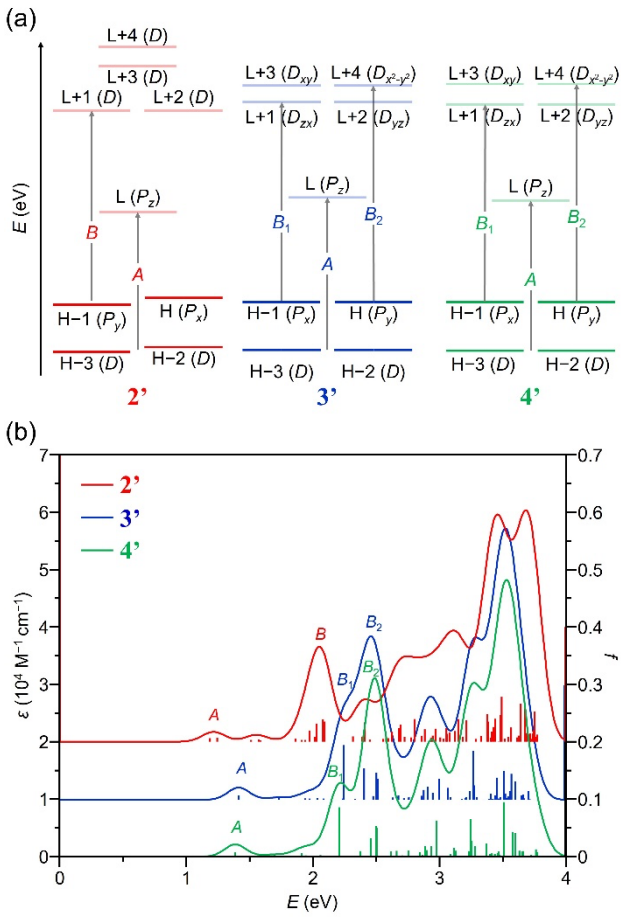

Figure 2. (a) Orbitals related to the optical absorption spectra and (b) calculated UV-vis-NIR spectra of **2'** (red), **3'** (blue), and **4'** (green). In (a), H and L indicate HOMO and LUMO, respectively. In (b), the baselines of **2'** and **3'** are shifted upward by 2 and 1 $\times 10^4$ M^{-1} cm^{-1}, respectively, to facilitate analysis.

The absorption spectra and orbitals of **2'** resembled those of $[Au_{24}Pt(C1)_{18}]^0$, which were previously reported.[6,35–37] Each of these three NCs had six valence electrons with LUMO, HOMO, and HOMO−1 frontier orbitals containing superatomic *P* and *D* orbital shapes (Figure **S11**). The predicted shapes of these orbitals, especially the characteristic superatomic orbitals distributed inside the $Au_{12}Pt$ cores, were similar for all three NCs. However, **3'** and **4'** had long chain-like staple morphologies connected by TDT or PDT moieties, which formed networks, leading to highly symmetric structures belonging to the D_3 point group (Scheme **1**). For this reason, both NCs exhibited significant orbital degeneracy (Figure **2a**).

Table **S2** summarizes the calculated vertical transitions of **2'**, **3'**, and **4'** in the low-energy region. The low-energy peak labeled A in the spectra of all NCs (Figure **2**) was attributed to the HOMO−2(*D*) or HOMO−3(*D*) to LUMO(P_z) transition. Transitions from HOMO or HOMO−1 to LUMO are forbidden because they involve transitions from one superatomic *P* orbital to another without changes in the angular momenta of the superatomic orbitals.[34] The *A* peak of **3'** was blue-shifted from that of **2'**. The peak labeled *B* was also blue-shifted to B_1 as a

consequence of TDT-based bridging (Figure **S11**). In the case of the experimental absorption spectrum, this peak was at approximately 2 eV and was also blue-shifted as a result of TDT bridging (Figure **1a and S9B**). Peak *B* was associated with several transitions, most notably the HOMO or HOMO−1 → LUMO+1 or LUMO+2 transitions (Table **S2**). Peak B_1 was also attributed to transitions between similar orbitals (Table **S2**). In contrast, newly emerged peak B_2 was attributed to the HOMO or HOMO−1 → LUMO+3 or LUMO+4 transition. The degenerate LUMO+3 and LUMO+4 orbitals of **3'** and **4'** were derived from the non-degenerate LUMO+3 and LUMO+4 orbitals of **2'** (Figure **2a**). The above findings established that TDT bridging produced orbital degeneracy as a consequence of symmetry enhancement and the stabilization of orbitals other than the LUMO, resulting in new absorption properties.

2.3. Single Crystal X-ray Diffraction Structures

The geometric structures of **3** and **4** were determined using SCXRD (refinement details are provided in Table **S3** and **S4**). Detailed structural analyses of **2**–**4** revealed that **3** and **4** had similar structures (Figures **3** and **S12**), both of which were significantly different from **2**. Specifically, all three possessed a 13 atom $Au_{12}Pt$ icosahedral core protected by Au-thiolate staple moieties. However, the size and orientation of these staples varied (Figure **3**). As an example, **2** had a total of six SR–Au–SR–Au–SR staples wrapped around its 13-atom icosahedral core. In contrast, **3** and **4** had two such staples joined by a dithiolate (TDT and PDT, respectively) to form a new, longer staple: S(R)–Au–S(R)–Au–**S–CH_2–(S or CH_2)–CH_2–S**–Au–S(R)–Au–S(R) (where R = 4-^{t}BuPh-). A total of three such staples were formed by three dithiolates (TDT or PDT).

Although **3** and **4** retained the icosahedral structure of **2**, the former two NCs displayed considerable distortion from an ideal icosahedral structure because of John–Teller effects originating in the partially filled non-degenerate *P* orbitals of the superatom electron configuration ($1S^21P^4$) of each NC.[35] The extent of distortion from an ideal icosahedron was assessed using the continuous symmetry measure (CSM) method implemented in SHAPE V2.1,[38,39] which provided CSM values of 0.073, 0.249, and 0.244 for **2**, **3**, and **4**, respectively (Figure **S13**). These data suggested that the latter two NCs comprised more distorted cores than **2**.

NC **2** contained two types of Au–Pt bonds with distances of 2.79 and 2.76 Å. This finding demonstrated that, among the 12 Pt–Au bonds, six bonds were elongated and the remaining six bonds were compressed to an equal extent (Figure **S14a** and Table **S5**).[6] In contrast, **3** had two equivalent Pt–Au bonds (2.79 Å), each with the same length as the longest Pt–Au bond in **2** (Figure **S14a** and Table **S5**). Among the remaining 10 Pt–Au bonds in **3**, two bonds (lengths of 2.75 Å) were more compressed than the other eight bonds (lengths between 2.78 and 2.76 Å). However, the difference between the shorter Pt–Au bonds (2.76 Å in **2** and 2.75 Å in **3**) was small (0.01 Å). The icosahedral core of **4** had six types of Au–Pt bonds with lengths of 2.75, 2.76, ~2.77, ~2.77, 2.78, and 2.79 Å (Figure **S14a** and Table **S5**), similar to **3**. Furthermore, the four longer and four shorter bonds of both **3** and **4** were similar in length, while the remaining four Pt−Au bonds of **4** were shorter than those of **3**. Therefore, the icosahedral core of **4** was more compressed than that of **3**. Overall, the order of icosahedral compression was estimated to be **2** > **4** > **3**, which differed from the trend described by the icosahedral distortion values (**3** > **4** > **2**; Figure **S13**).

Similarly, the Au–Au bonds in **2**–**4** varied in length (Figure **S14b** and Table **S5**). A plot of the Au–Au bond lengths (Figure **S14b**) revealed that **2** had a more ideal icosahedral core than **3** and **4**, both of which had similar cores with respect to Au–Au bond length and overall shape.

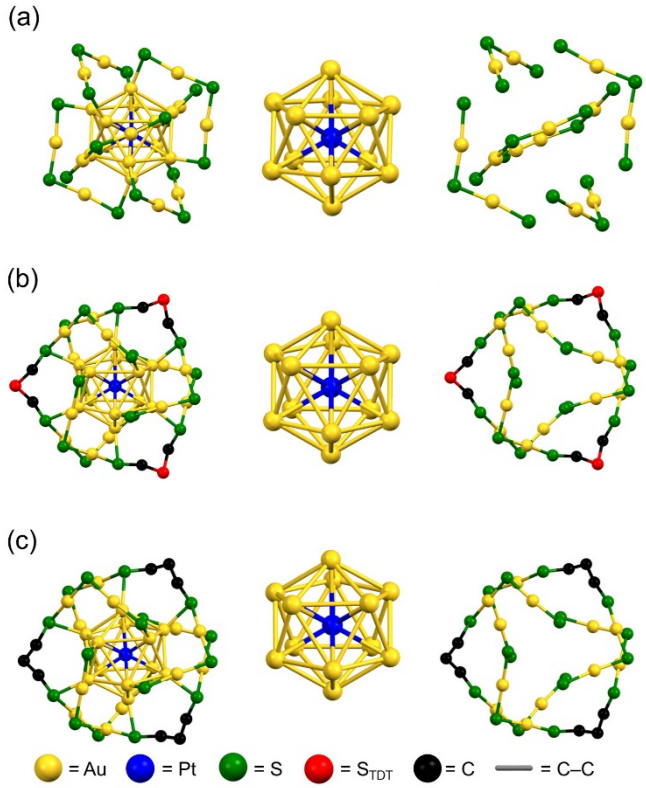

Figure 3. Comparison of geometric structures of **2**−**4**: Whole structures (left), core (middle), and staples (right) of (a) **2**, (b) **3**, and (c) **4**. All the carbon atoms of the TBBT ligand as well as all the H atoms of both TBBT and dithiolate ligands are not shown for clarity.

2.4. Importance of Alkyl Chain Length and Rigidity of Dithiolate-Ligands

Interestingly, all our efforts to synthesize homologues of **4**, such as $[Au_{24}Pt(TBBT)_{12}((S–(CH_2)_n–S))_3]^0$ (n = 2, 4 or 6), using alkyl dithiolate ligands of varying chain lengths resulted in a mixture of products, which precipitated as insoluble substances during the prolonged reaction or purification steps (Schemes **S6**−**S8** and Figures **S15**−**S17**). Precipitation occurred regardless of whether the reactions were conducted at room temperature or elevated temperatures under conditions similar to those used to synthesize **4**. These results suggest that there is an optimum dithiolate chain length for the high-yield synthesis of **4** or its homologues.

1,3-Benzenedithiol ($BDTH_2$) (Figure **S1g**) has the same number of carbons between the two –SH groups as $PDTH_2$, albeit in the form of a rigid benzene group. However, exchange reactions conducted with $BDTH_2$ at both room temperature and 60 °C failed to produce homologues of **4**, such as

$[Au_{24}Pt(TBBT)_{12}(BDT)_3]^0$ (Scheme **S9** and Figure **S18**), even when the $BDTH_2$ concentration was varied and the reaction time was increased. This outcome underscores the importance of optimizing both the length and flexibility of the carbon chain to enable the precise synthesis of dithiolate-containing NCs, such as **3** or **4**.

According to a previous study, an exchange reaction between $[Au_{25}(PET)_{18}]^-$ NCs and $PDTH_2$ yields a mixture of $Au_{25}(PET)_{18-2x}(PDT)_x$ NCs (x = 2–6) rather than a single main product, such as $[Au_{25}(PET)_{12}(PDT)_3]^-$.[40] By analyzing the NC mixture using matrix-assisted laser desorption ionization–MS and performing DFT calculations of a hypothetical $[Au_{25}(PDT)_9]^-$ NC, the authors predicted that an inter-staple PDT exchange between nearest core–apex positions preferentially occurs over an inter-staple exchange between nearest core–core positions. Interestingly, the present SCXRD analysis of $PDTH_2$-exchanged **4** resulted in an opposite trend to that obtained from the prior work described above. In the present study, each PDT moiety was preferentially connected to two nearest staples (RS–Au–SR–Au–SR, where SR = TBBT) through inter-staple core–core substitution (Figure **3**).

The preferential inter-staple core–core substitution of PDT observed in the case of **4** could be explained by considering the preferential substitution site for the incoming thiolates. Previous studies by the authors[41,42] on exchange reactions between chain-like C12 thiolate and $[Au_{24}Pd(PET)_{18}]^0$ showed that C12 preferentially exchanges with PET moieties at the core position to provide monosubstituted regioisomer $[Au_{24}Pd(PET)_{17}(C12)]^0$. Therefore, it is likely that the reaction between $PDTH_2$, which is a chain-like dithiol, and $[Au_{24}Pt(SR)_{18}]^0$ (SR = PET or TBBT) proceeds with the initial substitution of core-positioned PET or TBBT through one of its two thiolate groups to form intermediate NCs containing thiolate and dithiolate moieties, such as $[Au_{24}Pt(TBBT+PET)_{17}(PDTH)]^0$. Dangling Au–S–$CH_2CH_2CH_2$–SH groups in these NCs are immediately substituted by additional core-positioned PET or TBBT ligand in the nearest inter-staples to form $[Au_{24}Pt(TBBT+PET)_{16}(PDT)]^0$. A similar pathway also provides $[Au_{24}Pt(TBBT)_{14}(PDT)_2]^0$ (Figure **S19-S21** and Scheme **S10**) and $[Au_{24}Pt(TBBT)_{12}(PDT)_3]^0$, in which each PDT moiety was preferentially connected to two nearest staples through inter-staple core–core substitution.

We also attempted to produce $[Au_{24}Pt(TBBT)_{10}(PDT)_4]^0$ and $[Au_{24}Pt(TBBT)_8(PDT)_5]^0$ by controlling the reaction between **2** and $PDTH_2$. However, $[Au_{24}Pt(TBBT)_{10}(PDT)_4]^0$ was produced in low yield and $[Au_{24}Pt(TBBT)_8(PDT)_5]^0$ was produced in lower yield (Figure **S22**). Although **4** has six additional core sites for further $PDTH_2$ substitution, the distances between the core-positioned S of TBBT ligands (3.749, 3.897 and 4.022 Å) were too short for PDT bridging (~4.487 Å; Figure **S23**). Therefore, the staples in $[Au_{24}Pt(TBBT)_{10}(PDT)_4]^0$ and $[Au_{24}Pt(TBBT)_8(PDT)_5]^0$ were under considerable strain, which suppressed the production of $[Au_{24}Pt(TBBT)_{10}(PDT)_4]^0$ and $[Au_{24}Pt(TBBT)_8(PDT)_5]^0$, resulting in **4** as the main product.

2.5. Crucial Role of Thiolate Structure

To assess the effect of thiolate on the synthesis and properties of homologues of **4**, a new series of NCs, $[Au_{24}Pt(SR)_{12}(PDT)_3]^0$, was produced from $Au_{24}Pt(SR)_{18}$ (SR = C6 or PET) (Schemes **S11** and **S12**). Successful synthesis of $[Au_{24}Pt(SR)_{12}(PDT)_3]^0$ NCs was confirmed with the UV-vis spectra of these products, which were similar to that of **4** (Figures **S24** and **S25**). In particular, $[Au_{24}Pt(C6)_{12}(PDT)_3]^0$ was sufficiently stable to allow isolation and analysis of its composition by ESI-MS (Figure **S24**), although $[Au_{24}Pt(PET)_{12}(PDT)_3]^0$ completely decomposed/polymerized during washing an excess of $PDTH_2$ (Figure **S25**). Therefore, the structural characteristics of the SR moiety affects both the synthesis and stability of these novel $[Au_{24}Pt(SR)_{12}(PDT)_3]^0$ NCs.

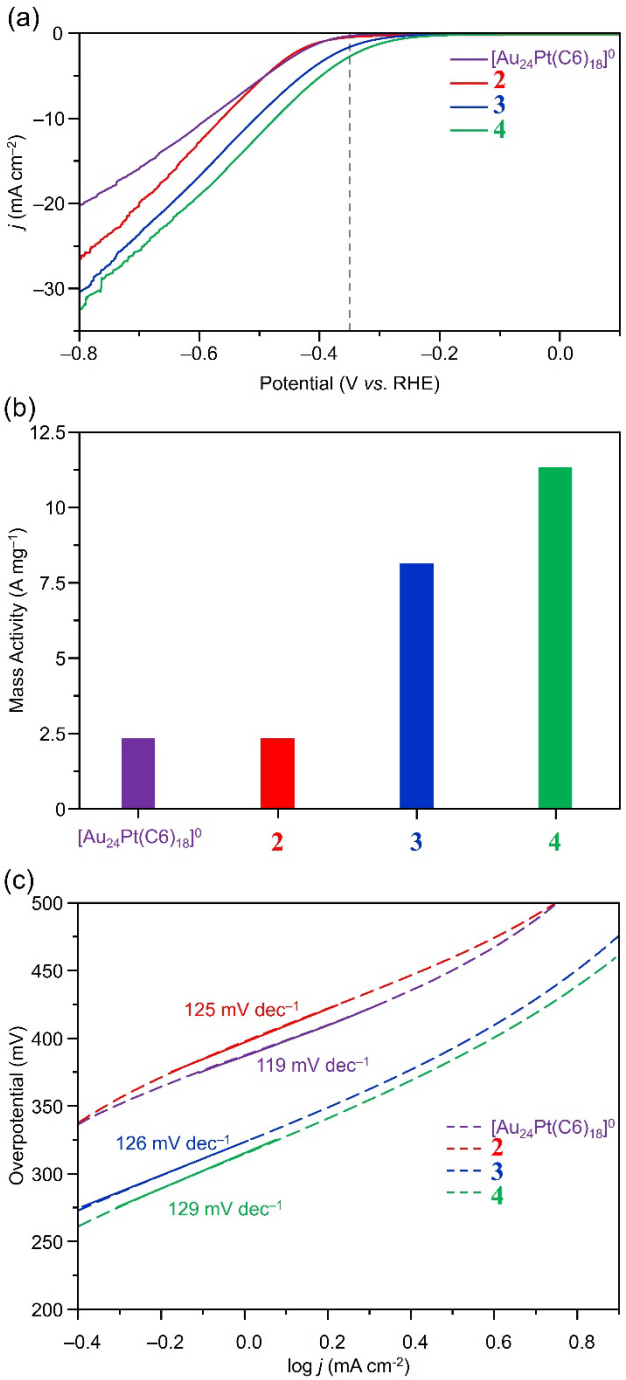

Figure 4. Comparison of the (a) LSV curves, (b) mass-based activities at −0.35 V *vs*. RHE, and (c) Tafel plots of $[Au_{24}Pt(C6)_{18}]^0$, **2**, **3**, and **4**.

2.6. Electrocatalytic Properties

In contrast to conventional $Au_{24}Pt(SR)_{18}$ NCs, **3** and **4** synthesized in the present work have only 12 TBBT ligands. The remaining six bulky TBBT ligands are replaced by three chain-like TDT or PDT dithiolate ligands. This reduction in the number of bulky ligands is expected to enhance catalytic activity by facilitating the access of reaction substrates to the active sites of **3** and **4**. Therefore, the HER activities of $[Au_{24}Pt(C6)_{18}]^0$ and **2**–**4** as representative $Au_{24}Pt$ NCs were evaluated by performing electrochemical measurements using CB loaded with these NCs. Au L_3-edge X-ray absorption fine structure and transmission electron microscopy assessments confirmed that the electronic/geometric structures of these NCs did not change during the catalyst preparation process (Figure **S26**).

The HER activities of these four specimens were subsequently investigated using linear sweep voltammetry (LSV) in 0.1 M aqueous $HClO_4$. During these trials, the current on the negative side was attributed to water reduction. Both NCs decreased the onset potential and current density (Figure **4a**), demonstrating that these materials promoted the HER. Furthermore, **3** and **4** increased the current density at a lower overpotential compared with $[Au_{24}Pt(C6)_{18}]^0$ and **2**. Specifically, the onset overpotentials in the presence of $[Au_{24}Pt(C6)_{18}]^0$ and **2**–**4** were 392, 396, 321, and 300 mV, respectively. Similarly, at the fixed overpotential of –0.35 V *vs*. RHE, the mass-based activities of **3** (8.15 A mg_{AuPt}^{-1}) and **4** (11.37 A mg_{AuPt}^{-1}) were, respectively, 3.5 and 4.9 times those of $[Au_{24}Pt(C6)_{18}]^0$ (2.35 A mg_{AuPt}^{-1}) and **2** (2.32 A mg_{AuPt}^{-1}) (Figure **4b**). These data unambiguously established that **3** and **4** were more efficient HER catalysts than $[Au_{24}Pt(C6)_{18}]^0$ and **2**. LSV data obtained with these materials after five scans are presented in Figure **S27**. These LSV curves almost overlapped at all scan numbers, indicating that $[Au_{24}Pt(C6)_{18}]^0$ and **2**–**4** promoted the HER in a stable manner (Figure **S27**). Our previous work[25] showed that the alkyl chain length has a significant impact on HER activity.[43] Hence, it was surprising to discover that **3** and **4** exhibited higher activities than $[Au_{24}Pt(C6)_{18}]^0$,[26,44] **1**, and **2**, despite their similar thiolate alkyl/aryl chain lengths.

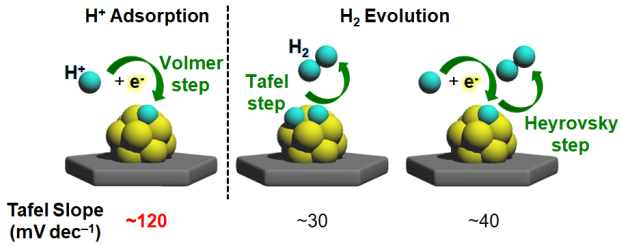

Figure 5. Mechanism by which a HER electrocatalyst promotes the two-step HER and Tafel slope value for each step.

To understand the origin of the high HER activity of **3** and **4**, Tafel plots (Figure **4c**) were generated from the corresponding LSV curves for each of the NCs (Figure **4a**). Although these materials provided considerably different onset potentials (Figure **4a**), $[Au_{24}Pt(C6)_{18}]^0$ and **2**–**4** provided similar Tafel slopes (119, 125, 126, and 129 mV/dec, respectively) (Figure **4c**). These values were close to the theoretical Tafel slope (120 mV/dec) of the Volmer step in the two-step HER (Figure **5**). Therefore, in the presence of all materials, the HER likely proceeds via a similar mechanism in which H^+ adsorption is the rate determining step (RDS). In the case of $[Au_{24}Pt(SR)_{18}]^0$, theoretical analyses have indicated that H^+ is adsorbed on the $Au_{12}Pt$ core.[45,46] Hence, the site of initial H^+ adsorption on $[Au_{24}Pt(SR)_{12}(dithiolate)_3]^0$ is likely the $Au_{12}Pt$ core. In the differential pulse voltammetry curves, the position of the 0/+1 redox peak of **2** shifted to the negative side compared with those of **3** and **4** (Figure **S28**). This indicates that the electronic structure of the $Au_{12}Pt$ core of **2** is more susceptible to oxidation[35] (accept H^+)[45] than those of **3** and **4**. However, the HER activities of **3** and **4** were higher than that of **2**. These results indicated that the difference in HER activities could not be explained by the difference in the electronic structures of **2**–**4**.

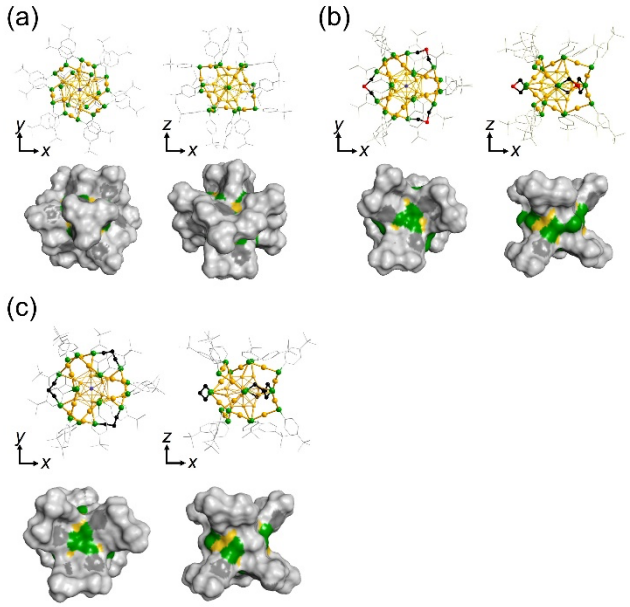

Figure 6. Exposed surface metal atoms (shown in gold) estimated using Discovery Studio 2021 Client for (a) **2**, (b) **3**, and (c) **4** shown from two different angles.

Here, it is helpful to consider the manner in which H^+ diffuses through the electrolyte to the $Au_{24}Pt$ surface because the $Au_{12}Pt$ core is the site of the HER. According to the proton jumping theory (namely the Grotthuss mechanism), H^+ diffuses through water by repeatedly forming and dissociating bonds between adjacent hydronium ions (H_3O^+) via a hydrogen-bond network.[47,48] Therefore, water molecules (H_3O^+) must penetrate the hydration structures (e.g., $H_5O_2^+$, $H_9O_4^+$, and $H_{13}O_6^+$)[49,50] by avoiding the hydrophobic R groups of the –SR ligands to reach the $Au_{12}Pt$ surface, where H^+ adsorption occurs.[45,46] Therefore, reducing the distance between the hydrated structure and the $Au_{12}Pt$ surface increases the rate of H^+ adsorption on the $Au_{12}Pt$ surface. As shown in Figure **6**, incorporating three –SCH_2–(S or CH_2)–CH_2S– ligands into **3** and **4** exposed the Au atoms of the metal core to a greater extent than was possible in **2.** As a result, the distance between the hydrated structure and the $Au_{12}Pt$ surface was significantly reduced, thereby facilitating proton transfer to the $Au_{12}Pt$ surface.[51] Increasing the rate of H^+ diffusion promotes H^+ adsorption and thus accelerates the HER. Indeed, introducing hydrophilic functional groups at the ends of the SR ligands of $Au_{24}Pt(SR)_{18}$ enhances the HER activity by promoting proton migration to the ligand surface.[52] Therefore, the high HER activities of **3** and **4** likely originate in their geometric structures, which promotes the adsorption of H^+ on the $Au_{12}Pt$ surface. We expect that the origin of the slight difference in the

HER activities of **3** and **4** would be revealed by investigating the diffusion of water molecules toward **3** and **4** through the hydration structures using molecular dynamics and TD-DFT calculations in future studies.

3. CONCLUSIONS

Two new Au–Pt alloy NCs were synthesized, and their geometric structures were determined using SCXRD. Detailed analyses of the syntheses and geometric structures of the products revealed that specific reaction conditions, including the reaction temperature and mixture of thiolate and dithiolate ligands, were required to produce these materials. In the performance trials, the HER activities of **3** and **4** were, respectively, 3.5 and 4.9 times those of $[Au_{24}Pt(C6)_{18}]^0$ and **2**, and this was explained by the greater exposure of surface Au atoms on the former, allowing easier access of H^+ to the HER-active $Au_{12}Pt$ core. Further investigations of the activities of these NCs as applied to the oxygen reduction reaction and carbon dioxide reduction reaction are currently underway in our laboratory.

4. EXPERIMENTAL

4.1. Chemicals

All chemicals were obtained commercially and used without further purification. Silver nitrate ($AgNO_3$), dimethyl sulfide, tetrahydrofuran (THF), trichloroethylene, methanol, toluene, hexane, dichloromethane, diethyl ether, acetonitrile, acetone, ethanol, and *n*-pentane were from Kanto Chemical Co. Triphenylphosphine (PPh_3), TBBTH (98%), silica gel 60N (spherical, neutral, particle size 63–210 μm), 2-propanol, and Nafion were from FUJIFILM Wako Pure Chemical Co. Sodium tetrahydroborate ($NaBH_4$), tetrakis(triphenylphosphine)platinum(0) ($Pt(PPh_3)_4$), triethylamine, TBBTH (97%), 1,2-etanedithiol, 1,3-propanedithiol ($PDTH_2$), 1,4-butanedithiol, 1,6-hexanedithiol, 1-hexanethiol, $BDTH_2$ and 1-propanethiol were from Tokyo Chemical Industry Co. 2-Phenylethanethiol (PETH) was from Sigma Aldrich. Hydrogen tetrachloroaurate(III) ($HAuCl_4$) tetrahydrate was from Tanaka Kikinzoku kogyo. Alumina N 32-63 was from MP Biomedicals. Pure Milli-Q H_2O (18.2 MΩ·cm) was generated using a Merck Millipore Direct 3 UV system.

4.2. Synthesis

$[Au_{24}Pt(PET)_{18}]^0$ (1). NC **1** was synthesized using a previously reported method with slight modifications.[30] First, 4.80 mmol of $HAuCl_4$ was dissolved in 10 mL of acetone, to which was added 10.6 mmol of PPh_3 dissolved in acetone, and the resulting solution was stirred at 0 °C for 15 min and filtered. The solution was then washed with acetone and dried to give $AuClPPh_3$. Resulting $AuClPPh_3$ was dissolved in dichloromethane, to which $AgNO_3$ was added, and the mixture was stirred in the dark for 1 h. The resulting product was purified to give $Au(NO_3)(PPh_3)$. Next, $Pt(PPh_3)_4$ was dissolved in ethanol, refluxed under argon for 2 h, and washed to obtain $Pt(PPh_3)_3$. $Au(NO_3)(PPh_3)$, synthesized earlier, was dissolved in THF and added to the solution, which was stirred under hydrogen for 3 h and allowed to stand for 6 h. The resulting product was quickly washed and dried under vacuum. The dried product was dissolved in dichloromethane, to which triethylamine and $Au(NO_3)(PPh_3)$ were added, and the mixture was stirred overnight. The resulting product was dried using a rotary evaporator, dissolved in methanol, and crystallized by adding diethyl ether as a poor solvent. The resulting crystals were washed with diethyl ether and *n*-pentane and solidified to dryness to give $[PtAu_8(PPh_3)_8](NO_3)_2$. Then, $[PtAu_8(PPh_3)_8](NO_3)_2$ was dissolved in ethanol and 500 μL of 0.1 M $NaBH_4$ ethanol solution. $AuCl(S(CH_3)_2)$ was obtained by dissolving $HAuCl_4$ in methanol, to which was added dimethyl sulfide and 900 μmol of PETH in THF, and the mixture was stirred for 30 min. Next, 1.20 mmol of triethylamine dissolved in THF was added, and the mixture was stirred for 30 min. The product was washed and purified on an alumina column (dichloromethane:hexane = 1:1) to give NC **1** (Scheme **S1**).

$[Au_{24}Pt(TBBT)_{18}]^0$ (2). NC **2** was synthesized using a previously reported method with slight modifications.[26] After dissolving 5.0 mg of NC **1** in 3.4 mL of toluene, 500 μL of TBBTH (98%, FUJIFILM) was added to the solution at 60 °C, and the mixture was stirred for 1.5 h to allow the ligand exchange reaction to proceed. The resulting product was washed with ultrapure water and a mixture of ultrapure water and methanol and extracted with dichloromethane. Finally, the products were separated by PTLC (dichloromethane:hexane = 7:13), and the top layer was scraped off and dissolved in dichloromethane to give NC **2** (Scheme **S2**). The optical absorption spectrum of this product matched that of NC **2**, which we reported in an earlier publication, and the ESI spectrum confirmed the presence of NC **2** as the main product, indicating that the same product was synthesized through the present modified method (Figure **S1**).

$[Au_{24}Pt(TBBT)_{12}(TDT)_3]^0$ (3). First, 5.0 mg of NC **1** was dissolved in 3.4 mL of toluene, to which 500 μL of TBBTH (97%, Tokyo Chemical Industry) was added at 60 °C, and the mixture was stirred for 1.5 h to allow the ligand exchange reaction to proceed. The resulting product was washed with ultrapure water and a mixture of ultrapure water and methanol and extracted with dichloromethane. Finally, the products were separated by PTLC (dichloromethane:hexane = 7:13), and the top layer was scraped off and dissolved in dichloromethane to obtain NC **3** (Scheme **1** and **S3**).

$[Au_{24}Pt(TBBT)_{12}(PDT)_3]^0$ (4). The exchange of thiol (RSH) ligands on Au NCs with aliphatic dithiol ligands (such as $HS(CH_2)_xSH$, where *x* is an integer) can lead to polymerization. This occurs because the carbon backbone of the latter is flexible and these ligands readily form strong inter-cluster Au–S or S–S bonds (such as **Au**–**S**$(CH_2)_x$**S**–**Au** or Au–S$(CH_2)_x$**S**–**S**$(CH_2)_x$S–Au).[53] Hence, it was necessary to optimize the ratio of **1** to the reacting thiols in addition to the thiol concentration. In the optimized synthesis, 5.0 mg of **1** was dissolved in 3.4 mL of toluene, to which 486 μL of TBBTH (98%) and 14.5 μL of $PDTH_2$ were added at 60 °C, and the mixture was stirred for 1.5 h to allow the ligand exchange reaction to proceed. The resulting product was washed with ultrapure water and a mixture of ultrapure water and methanol sequentially and extracted with dichloromethane. Finally, the products were separated by PTLC (dichloromethane:hexane = 7:13), and the top layer was scraped off and extracted with dichloromethane to obtain NC **4** (Scheme **1** and **S5**).

4.3. Preparation of $Au_{24}Pt$ NC/CB (1.0 wt% metal)

An impregnation method was employed to make $Au_{24}Pt$ NC/CB (1.0 wt% metal). A dichloromethane solution of $Au_{24}Pt$ NCs was dropped on the CB and then dried.

4.4. Preparation of catalyst slurry

For the electrochemical measurements using $Au_{24}Pt$ NC/CB(1.0 wt% metal), we prepared a catalyst slurry. First, a dried powder of the catalyst (10.1 mg of $Au_{24}Pt$ NC/CB; 1.0 wt% metal) was dispersed in a solution of H_2O (19.1 mL) and 2-propanol (6.0 mL), to which a Nafion solution (100 μL) was added. Finally, the mixture was sonicated for 60 mins in an ice bath while sealed in a reaction vial.

4.5. Electrochemical measurements

All electrochemical measurements of the HER were performed with an ECstat-302 (EC FRONTIER, Kyoto, Japan) and RRDE-3A rotating ring disk electrode apparatus (BAS, Tokyo, Japan). A rotating disk electrode (RDE, φ = 5 mm, glassy carbon) was cleaned before use. Specifically, it was polished with alumina paste and then sonicated in water. Pt coil and Ag/AgCl electrodes were used as counter and reference electrodes, respectively. In the setup, the catalyst slurry was homogenized. Specifically, it was sonicated in an ice bath for 30 min. Then, 10 μL of the slurry was carefully dropped onto the RDE and rotated in open air until it dried. Next, each electrode was placed in 0.10 mol L^{-1} $HClO_4$ (pH = 1.0) electrolyte attached to an electrochemical measurement system. The electrode surface was then cleaned by bubbling N_2 gas for 30 min. Then, cyclic voltammetry (CV) was performed 100 times in the region of 0.00 to −1.00 V (vs. RHE) at a scanning rate of 200 mV/s. Finally, LSV was performed in the region of 0.20 to –0.80 V (vs. RHE) at a rate of 20 mV/s under N_2 gas.

5. THEORETICAL CALCULATIONS

Density functional theory (DFT) and time-dependent (TD) DFT calculations were performed using Gaussian 16 (ES64L-G16, RevB.01)[54] to elucidate the electronic structures of $[Au_{24}Pt(TBBT)_{18}]^0$, $[Au_{24}Pt(TBBT)_{12}(TDT)_3]^0$, and $[Au_{24}Pt(TBBT)_{12}(PDT)_3]^0$. The structures obtained from the SCXRD of each molecule were used as the initial structures, with TBBT replaced by methanethiolate (SMe) to reduce the calculation cost. No changes were made to the TDT and PDT moieties. The BP86 functional[55] was used to optimize the structure of ground state S_0, and the basis sets were Def2-SVPP (for Au and Pt)[56] and 6-31G(d,p) (for S,C, and H)[57]. For metal atoms, we incorporated SDD pseudopotentials with scalar relativistic effect[58]. The absence of imaginary frequencies was confirmed by vibration analysis. Next, the vertical transition from S_0 to S_n (n = 1−150) was calculated at the TD-B3LYP functional level for the obtained S_0-optimized structure.[59–61] The same basis sets and pseudopotentials were used for structural optimization. Absorption spectra were reproduced with a width of σ = 800 cm^{-1} using bar spectra obtained from single-point calculations. Molecular orbitals were visualized using Avogadro.

ASSOCIATED CONTENT

Supporting Information. Additional synthesis methods, electrochemical measurement methods, characterization, crystal data of samples and other Au NCs, additional information of geometric structure, additional schemes, ESI-MS spectra, UV-vis optical absorption spectra, HPLC, PTLC, crystallization, MALDI-MS spectra, FT-XAFS and XANES spectra, TEM image, stability test of LSV, and DPV curves. This material is available free of charge via the Internet at http://pubs.acs.org.

AUTHOR INFORMATION

Corresponding Author

Sakiat Hossain - Research Institute for Science & Technology, Tokyo University of Science, Kagurazaka, Shinjuku-ku, Tokyo 162-8601, Japan; E-mail: hisakiat@gmail.com; Orcid: https://orcid.org/0000-0003-4075-6980

Yuichi Negishi - Institute of Multidisciplinary Research for Advanced Materials, Tohoku University, Katahira 2-1-1, Aoba-ku, Sendai 980-8577, Japan; Orcid: https://orcid.org/0000-0003-3965-1399; E-mail: yuichi.negishi.a8@tohoku.ac.jp

Authors

Miyu Sera - Department of Applied Chemistry, Faculty of Science, Tokyo University of Science, Kagurazaka, Shinjuku-ku, Tokyo 162-8601, Japan

Sara Yoshikawa - Department of Applied Chemistry, Faculty of Science, Tokyo University of Science, Kagurazaka, Shinjuku-ku, Tokyo 162-8601, Japan

Kana Takemae - Department of Applied Chemistry, Faculty of Science, Tokyo University of Science, Kagurazaka, Shinjuku-ku, Tokyo 162-8601, Japan

Ayaka Ikeda - Department of Applied Chemistry, Faculty of Science, Tokyo University of Science, Kagurazaka, Shinjuku-ku, Tokyo 162-8601, Japan

Tomoya Tanaka - Department of Applied Chemistry, Faculty of Science, Tokyo University of Science, Kagurazaka, Shinjuku-ku, Tokyo 162-8601, Japan

Taiga Kosaka - Department of Applied Chemistry, Faculty of Science, Tokyo University of Science, Kagurazaka, Shinjuku-ku, Tokyo 162-8601, Japan

Yoshiki Niihori - Research Institute for Science & Technology, Tokyo University of Science, Kagurazaka, Shinjuku-ku, Tokyo 162-8601, Japan; Orcid: https://orcid.org/0000-0002-6147-3464

Tokuhisa Kawawaki - Department of Applied Chemistry, Faculty of Science, Tokyo University of Science, Kagurazaka, Shinjuku-ku, Tokyo 162-8601, Japan; Research Institute for Science & Technology, Tokyo University of Science, Kagurazaka, Shinjuku-ku, Tokyo 162-8601, Japan; Orcid: https://orcid.org/0000-0003-3282-8964

Author Contributions

Y. Negishi and S.H. designed the experiments and conducted the measurements along with M.S., S.Y., A.I., and T. Kawawaki; T. Kosaka and Y. Niihori performed the DFT calculations; K.T. and T.T. performed the applications; Y. Negishi and S.H. wrote the paper. All authors have approved the final version of the manuscript.

ACKNOWLEDGMENT

We thank Prof. Häkkinen (University of Jyväskylä) for the discussion on DFT calculation and Ms Akiyama, Ms Ishimi, Mr Shingyouchi and Mr Ogami for helping the experiments. This study was supported by the Japan Society for the Promotion of Science (JSPS) KAKENHI (grant no. 22K19012 and 23H00289), Scientific Research on Innovative Areas “Aquatic Functional

Materials" (grant no. 22H04562), Yazaki Memorial Foundation for Science and Technology, Ogasawara Foundation for the Promotion of Science and Engineering, Iwatani Naoji Foundation, Ichimura Foundation for New Technology, Suzuki Foundation, and Japan Keirin Autorace foundation.

ABBREVIATIONS

HER, hydrogen evolution reaction, C6, 1-hexanethiolate, CB, Vulcan carbon black, PET, 2-phenylethanethiolate, TBBT, 4-tert-butylbenzenethiolate, TDT, thiodithiolate, PDT, 1,3-propanedithiolate, SCXRD, single crystal X-ray diffraction, UV-vis-NIR, ultraviolet-visible-near infrared, DFT, density functional theory, HOMO, highest occupied molecular orbital, LUMO, lowest unoccupied molecular orbital, PTLC, preparative thin-layer chromatography, ESI-MS, electrospray ionization-mass spectrometry, RP-HPLC, reverse-phase high-performance liquid chromatography

REFERENCES

(1) Hydrogen Basics. United States Department of Energy. https://afdc.energy.gov/fuels/hydrogen_basics.html (accessed 2024-03-27).

(2) Hydrogen Production and Distribution. United States Department of Energy. https://afdc.energy.gov/fuels/hydrogen_production.html (accessed 2024-03-27).

(3) Howarth, R. W.; Jacobson, M. Z. How Green Is Blue Hydrogen? *Energy Sci. Eng.* **2021**, *9*, 1676‑1687. DOI: 10.1002/ese3.956

(4) Li, C.; Baek, J.-B. Recent Advances in Noble Metal (Pt, Ru, and Ir)-Based Electrocatalysts for Efficient Hydrogen Evolution Reaction. *ACS Omega* **2020**, *5*, 31–40. DOI: 10.1021/acsomega.9b03550

(5) Li, M.; Duanmu, K.; Wan, C.; Cheng, T.; Zhang, L.; Dai, S.; Chen, W.; Zhao, Z.; Li, P.; Fei, H.; Zhu, Y.; Yu, R.; Luo, J.; Zang, K.; Lin, Z.; Ding, M.; Huang, J.; Sun, H.; Guo, J.; Pan, X.; Goddard III, W. A.; Sautet, P.; Huang, Y.; Duan, X. Single-atom Tailoring of Platinum Nanocatalysts for High-Performance Multifunctional Electrocatalysis. *Nat. Catal.* **2019**, *2*, 495–503. DOI: 10.1038/s41929-019-0279-6

(6) Kwak, K.; Choi, W.; Tang, Q.; Kim, M.; Lee, Y.; Jiang, D.-e.; Lee, D. A Molecule-Like $PtAu_{24}(SC_6H_{13})_{18}$ Nanocluster as an Electrocatalyst for Hydrogen Production. *Nat. Commun.* **2017**, *8*, 14723. DOI: 10.1038/ncomms14723

(7) Narouz, M. R.; Osten, K. M.; Unsworth, P. J.; Man, R. W. Y.; Salorinne, K.; Takano, S.; Tomihara, R.; Kaappa, S.; Malola, S.; Dinh, C.-T.; Padmos, J. D.; Ayoo, K.; Garrett, P. J.; Nambo, M.; Horton, J. H.; Sargent, E. H.; Häkkinen, H.; Tsukuda, T.; Crudden, C. M. N-Heterocyclic Carbene-Functionalized Magic-Number Gold Nanoclusters. *Nat. Chem.* **2019**, *11*, 419–425. DOI: 10.1038/s41557-019-0246-5

(8) Jin, R.; Zeng, C.; Zhou, M.; Chen, Y. Atomically Precise Colloidal Metal Nanoclusters and Nanoparticles: Fundamentals and Opportunities. *Chem. Rev.* **2016**, *116*, 10346–10413. DOI: 10.1021/acs.chemrev.5b00703

(9) Chakraborty, I.; Pradeep, T. Atomically Precise Clusters of Noble Metals: Emerging Link between Atoms and Nanoparticles. *Chem. Rev.* **2017**, *117*, 8208–8271. DOI: 10.1021/acs.chemrev.6b00769

(10) Ganguly, A.; Chakraborty, I.; Udayabhaskararao, T.; Pradeep, T. A Copper Cluster Protected with Phenylethanethiol. *J. Nanopart. Res.* **2013**, *15*, 1522. DOI: 10.1007/s11051-013-1522-8

(11) Heaven, M. W.; Dass, A.; White, P. S.; Holt, K. M.; Murray, R. W. Crystal Structure of the Gold Nanoparticle $[N(C_8H_{17})_4][Au_{25}(SCH_2CH_2Ph)_{18}]$. *J. Am. Chem. Soc.* **2008**, *130*, 3754–3755. DOI: 10.1021/ja800561b

(12) Jiang, D.-e.; Dai, S. From Superatomic $Au_{25}(SR)_{18}^-$ to Superatomic $M@Au_{24}(SR)_{18}^q$ Core–Shell Clusters. *Inorg. Chem.* **2009**, *48*, 2720–2722. DOI: 10.1021/ic8024588

(13) Tofanelli, M. A.; Salorinne, K.; Ni, T. W.; Malola, S.; Newell, B.; Phillips, B.; Häkkinen, H.; Ackerson, C. J. Jahn–Teller Effects in $Au_{25}(SR)_{18}$. *Chem. Sci.* **2016**, *7*, 1882–1890. DOI: 10.1039/C5SC02134K

(14) Yao, Q.; Yuan, X.; Fung, V.; Yu, Y.; Leong, D. T.; Jiang, D.-e.; Xie, J. Understanding Seed-Mediated Growth of Gold Nanoclusters at Molecular Level. *Nat. Commun.* **2017**, *8*, 927. DOI: 10.1038/s41467-017-00970-1

(15) Jin, R.; Li, G.; Sharma, S.; Li, Y.; Du, X. Toward Active-Site Tailoring in Heterogeneous Catalysis by Atomically Precise Metal Nanoclusters with Crystallographic Structures. *Chem. Rev.* **2021**, *121*, 567–648. DOI: 10.1021/acs.chemrev.0c00495

(16) Fang, J.; Zhang, B.; Yao, Q.; Yang, Y.; Xie, J.; Yan, N. Recent Advances in the Synthesis and Catalytic Applications of Ligand-Protected, Atomically Precise Metal Nanoclusters. *Coord. Chem. Rev.* **2016**, *322*, 1–29. DOI: 10.1016/j.ccr.2016.05.003

(17) Kawasaki, H.; Kumar, S.; Li, G.; Zeng, C.; Kauffman, D. R.; Yoshimoto, J.; Iwasaki, Y.; Jin, R. Generation of Singlet Oxygen by Photoexcited $Au_{25}(SR)_{18}$ Clusters. *Chem. Mater.* **2014**, *26*, 2777–2788. DOI: 10.1021/cm500260z

(18) Knoppe, S.; Bürgi, T. Chirality in Thiolate-Protected Gold Clusters. *Acc. Chem. Res.* **2014**, *47*, 1318–1326. DOI: 10.1021/ar400295d

(19) Li, S.; Li, N.-N.; Dong, X.-Y.; Zang, S.-Q.; Mak, T. C. W. Chemical Flexibility of Atomically Precise Metal Clusters. *Chem. Rev.* **2024**, *124*, 7262–7378. DOI: 10.1021/acs.chemrev.3c00896

(20) Qian, H.; Jiang, D.-e.; Li, G.; Gayathri, C.; Das, A.; Gil, R. R.; Jin, R. Monoplatinum Doping of Gold Nanoclusters and Catalytic Application. *J. Am. Chem. Soc.* **2012**, *134*, 16159–16162. DOI: 10.1021/ja307657a

(21) Yang, H.; Wang, Y.; Yan, J.; Chen, X.; Zhang, X.; Häkkinen, H.; Zheng, N. Structural Evolution of Atomically Precise Thiolated Bimetallic $[Au_{12+n}Cu_{32}(SR)_{30+n}]^{4-}$ (n = 0, 2, 4, 6) Nanoclusters. *J. Am. Chem. Soc.* **2014**, *136*, 7197–7200. DOI: 10.1021/ja501811j

(22) Yoskamtorn, T.; Yamazoe, S.; Takahata, R.; Nishigaki, J.-i.; Thivasasith, A.; Limtrakul, J.; Tsukuda, T. Thiolate-Mediated Selectivity Control in Aerobic Alcohol Oxidation by Porous Carbon-Supported Au_{25} Clusters. *ACS Catal.* **2014**, *4*, 3696–3700. DOI: 10.1021/cs501010x

(23) Zhang, B.; Kaziz, S.; Li, H.; Hevia, M. G.; Wodka, D.; Mazet, C.; Bürgi, T.; Barrabés, N. Modulation of Active Sites in Supported $Au_{38}(SC_2H_4Ph)_{24}$ Cluster Catalysts: Effect of Atmosphere and Support Material. *J. Phys. Chem. C* **2015**, *119*, 11193–11199. DOI: 10.1021/jp512022v

(24) Lei, Z.; Li, J.-J.; Nan, Z.-A.; Jiang, Z.G.; Wang, Q.-M. Cluster From Cluster: A Quantitative Approach to Magic Gold Nanoclusters $[Au_{25}(SR)_{18}]^-$. *Angew. Chem.* **2021**, *133*, 14536–14540. DOI: 10.1002/anie.202103290

(25) Kumar, B.; Kawawaki, T.; Shimizu, N.; Imai, Y.; Suzuki, D.; Hossain, S.; Nair, L. V.; Negishi, Y. Gold Nanoclusters as Electrocatalysts: Size, Ligands, Heteroatom Doping, and Charge Dependences. *Nanoscale* **2020**, *12*, 9969–9979. DOI: 10.1039/D0NR00702A

(26) Hossain, S.; Imai, Y.; Suzuki, D.; Choi, W.; Chen, Z.; Suzuki, T.; Yoshioka, M.; Kawawaki, T.; Lee, D.; Negishi, Y. Elucidating Ligand Effects in Thiolate-Protected Metal Clusters Using $Au_{24}Pt(TBBT)_{18}$ as a Model Cluster. *Nanoscale* **2019**, *11*, 22089–22098. DOI: 10.1039/C9NR07117B

(27) Negishi, Y.; Horihata, H.; Ebina, A.; Miyajima, S.; Nakamoto, M.; Ikeda, A.; Kawawaki, T.; Hossain, S. Selective Formation of $[Au_{23}(SPh^tBu)_{17}]^0$, $[Au_{26}Pd(SPh^tBu)_{20}]^0$ and $[Au_{24}Pt(SC_2H_4Ph)_7(SPh^tBu)_{11}]^0$ by Controlling Ligand-Exchange Reaction. *Chem. Sci.* **2022**, *13*, 5546–5556. DOI: 10.1039/C9NR07117B

(28) Sels, A.; Salassa, G.; Pollitt, S.; Guglieri, C.; Rupprechter, G.; Barrabés, N.; Bürgi, T. Structural Investigation of the Ligand Exchange Reaction with Rigid Dithiol on Doped (Pt, Pd) Au_{25} Clusters. *J. Phys. Chem. C* **2017**, *121*, 10919–10926. DOI: 10.1021/acs.jpcc.6b12066

(29) Zhang, S.-S.; Feng, L.; Senanayake, R. D.; Aikens, C. M.; Wang, X.-P.; Zhao, Q.-Q.; Tung, C.-H.; Sun, D. Diphosphine-Protected Ultrasmall Gold Nanoclusters: Opened Icosahedral Au_{13} and Heart-Shaped Au_8 Clusters. *Chem. Sci.* **2018**, *9*, 1251–1258. DOI: 10.1039/C7SC03566G

(30) Takano, S.; Ito, S.; Tsukuda, T. Efficient and Selective Conversion of Phosphine-Protected $(MAu_8)^{2+}$ (M = Pd, Pt) Superatoms to Thiolate-Protected $(MAu_{12})^{6+}$ or Alkynyl-Protected $(MAu_{12})^{4+}$ Superatoms via Hydride Doping. *J. Am. Chem. Soc.* **2019**, *141*, 15994–16002. DOI: 10.1021/jacs.9b08055

(31) Chen, Y.; Zeng, C.; Kauffman, D. R.; Jin, R. Tuning the Magic Size of Atomically Precise Gold Nanoclusters via Isomeric Methylbenzenethiols. *Nano Lett.* **2015**, *15*, 3603–3609. DOI: 10.1021/acs.nanolett.5b01122

(32) Yang, H.; Wang, Y.; Edwards, A. J.; Yan, J.; Zheng, N. High-Yield Synthesis and Crystal Structure of a Green Au_{30} Cluster Co-Capped by Thiolate and Sulfide. *Chem. Commun.* **2014**, *50*, 14325–14327. DOI: 10.1039/C4CC01773K

(33) Fan, W.; Yan, N.; Zha, J.; Gu, W.; You, Q.; Yang, Y.; Zhuang, S.; Wu, Z. Regulating the Electronic Structure of Metal Nanoclusters by Longitudinal Single-Dithiolate Substitution. *J. Phys. Chem. Lett.* **2023**, *14*, 3216–3221. DOI: 10.1021/acs.jpclett.3c00238

(34) D'Antoni, P.; Sementa, L.; Bonacchi, S.; Reato, M.; Maran, F.; Fortunelli, A.; Stener, M. Combined Experimental and Computational Study of the Photoabsorption of the Monodoped and Nondoped Nanoclusters $Au_{24}Pt(SR)_{18}$, $Ag_{24}Pt(SR)_{18}$, and $Ag_{25}(SR)_{18}$. *Phys. Chem. Chem. Phys.* **2024**, *26*, 17569–17576. DOI: 10.1039/D4CP00789A

(35) Kwak, K.; Tang, Q.; Kim, M.; Jiang, D.-e.; Lee, D. Interconversion between Superatomic 6-Electron and 8-Electron Configurations of $M@Au_{24}(SR)_{18}$ Clusters (M = Pd, Pt). *J. Am. Chem. Soc.* **2015**, *137*, 10833–10840. DOI: 10.1021/jacs.5b06946

(36) Hossain, S.; Ono, T.; Yoshioka, M.; Hu, G.; Hosoi, M.; Chen, Z.; Nair, L. V.; Niihori, Y.; Kurashige, W.; Jiang, D.-e.; Negishi, Y. Thiolate-Protected Trimetallic $Au_{\sim 20}Ag_{\sim 4}Pd$ and $Au_{\sim 20}Ag_{\sim 4}Pt$ Alloy Clusters with Controlled Chemical Composition and Metal Positions. *J. Phys. Chem. Lett.* **2018**, *9*, 2590–2594. DOI: 10.1021/acs.jpclett.8b00910

(37) Zhu, M.; Aikens, C. M.; Hollander, F. J.; Schatz, G. C.; Jin, R. Correlating the Crystal Structure of a Thiol-Protected Au_{25} Cluster and Optical Properties. *J. Am. Chem. Soc.* **2008**, *130*, 5883–5885. DOI: 10.1021/ja801173r

(38) Zabrodsky, H.; Peleg, S.; Avnir, D. Continuous Symmetry Measures. *J. Am. Chem. Soc.* **1992**, *114*, 7843–7851. DOI: 10.1021/ja00046a033

(39) Echeverría, J.; Casanova, D.; Llunell, M.; Alemany, P.; Alvarez, S. Molecules and Crystals with Both Icosahedral and Cubic Symmetry. *Chem. Commun.* **2008**, 2717–2725. DOI: 10.1039/B719615F

(40) Jupally, V. R.; Kota, R.; Dornshuld, E. V.; Mattern, D. L.; Tschumper, G. S.; Jiang, D.-e.; Dass, A. Interstaple Dithiol Cross-Linking in $Au_{25}(SR)_{18}$ Nanomolecules: A Combined Mass Spectrometric and Computational Study. *J. Am. Chem. Soc.* **2011**, *133*, 20258–20266. DOI: 10.1021/ja206436x

(41) Niihori, Y.; Kikuchi, Y.; Kato, A.; Matsuzaki, M.; Negishi, Y. Understanding Ligand-Exchange Reactions on Thiolate-Protected Gold Clusters by Probing Isomer Distributions Using Reversed-Phase High-Performance Liquid Chromatography. *ACS Nano* **2015**, *9*, 9347–9356. DOI: 10.1021/acsnano.5b03435

(42) Niihori, Y.; Kurashige, W.; Matsuzaki, M.; Negishi, Y. Remarkable Enhancement in Ligand-Exchange Reactivity of Thiolate-Protected Au_{25} Nanoclusters by Single Pd atom Doping. *Nanoscale* **2013**, *5*, 508–512. DOI: 10.1039/C2NR32948D

(43) Li, B.; Kang, L.; Lun, Y.; Yu, J.; Song, S.; Wang, Y. Structure–performance Relationship of Au Nanoclusters in Electrocatalysis: Metal Core and Ligand Structure. *Carbon Energy.* **2024**, e547. DOI: 10.1002/cey2.547

(44) Choi, W.; Hu, G.; Kwak, K.; Kim, M.; Jiang, D.-e.; Choi, J.-P.; Lee, D. Effects of Metal-Doping on Hydrogen Evolution Reaction Catalyzed by MAu_{24} and M_2Au_{36} Nanoclusters (M = Pt, Pd). *ACS Appl. Mater. Interfaces* **2018**, *10*, 44645–44653. DOI: 10.1021/acsami.8b16178

(45) López-Estrada, O.; Mammen, N.; Laverdure, L.; Melander, M. M.; Häkkinen, H.; Honkala, K. Computational Criteria for Hydrogen Evolution Activity on Ligand-Protected Au_{25}-Based Nanoclusters. *ACS Catal.* **2023**, *13*, 8997–9006. DOI: 10.1021/acscatal.3c01065

(46) Hu, G.; Tang, Q.; Lee, D.; Wu, Z.; Jiang, D.-e. Metallic Hydrogen in Atomically Precise Gold Nanoclusters. *Chem. Mater.* **2017**, *29*, 4840–4847. DOI: 10.1021/acs.chemmater.7b00776

(47) Kreuer, K.-D.; Paddison, S. J.; Spohr, E.; Schuster, M. Transport in Proton Conductors for Fuel-Cell Applications: Simulations, Elementary Reactions, and Phenomenology. *Chem. Rev.* **2004**, *104*, 4637–4678. DOI: 10.1021/cr020715f

(48) Calio, P. B.; Li, C.; Voth, G. A. Resolving the Structural Debate for the Hydrated Excess Proton in Water. *J. Am. Chem. Soc.* **2021**, *143*, 18672–18683. DOI: 10.1021/jacs.1c08552

(49) Kundu, A.; Dahms, F.; Fingerhut, B. P.; Nibbering, E. T. J.; Pines, E.; Elsaesser, T. Hydrated Excess Protons in Acetonitrile/Water Mixtures: Solvation Species and Ultrafast Proton Motions. *J. Phys. Chem. Lett.* **2019**, *10*, 2287–2294. DOI: 10.1021/acs.jpclett.9b00756

(50) Stoyanov, E. S.; Stoyanova, I. V.; Reed, C. A. The Structure of the Hydrogen Ion (H_{aq}^+) in Water. *J. Am. Chem. Soc.* **2010**, *132*, 1484–1485. DOI: 10.1021/ja9101826

(51) Li, X.-Y.; Wang, T.; Cai, Y.-C.; Meng, Z.-D.; Nan, J.-W.; Ye, J.-Y.; Yi, J.; Zhan, D.-P.; Tian, N.; Zhou, Z.-Y.; Sun, S.-G. Mechanism of Cations Suppressing Proton Diffusion Kinetics for Electrocatalysis. *Angew. Chem., Int. Ed.* **2023**, *62*, e202218669. DOI: 10.1002/anie.202218669

(52) Kwak, K.; Choi, W.; Tang, Q.; Jiang, D.-e.; Lee, D. Rationally Designed Metal Nanocluster for Electrocatalytic Hydrogen Production from Water. *J. Mater. Chem. A* **2018**, *6*, 19495–19501. DOI: 10.1039/C8TA06306K

(53) Saito, Y.; Shichibu, Y.; Konishi, K. Self-promoted Solid-state Covalent Networking of $Au_{25}(SR)_{18}$ through Reversible Disulfide Bonds. A Critical Effect of the Nanocluster in Oxidation Processes. *Nanoscale* **2021**, *13*, 9971–9977. DOI: 10.1039/D1NR01812D

(54) Frisch, M. J.; Trucks, G. W.; Schlegel, H. B.; Scuseria, G. E.; Robb, M. A.; Cheeseman, J. R.; Scalmani, G.; Barone, V.; Petersson, G. A.; Nakatsuji, H.; Li, X.; Caricato, M.; Marenich, A. V.; Bloino, J.; Janesko, B. G.; Gomperts, R.; Mennucci,; B.; Hratchian, H. P.; Ortiz, J. V.; Izmaylov, A. F.; Sonnenberg, J. L.; Williams-Young, D.; Ding, F.; Lipparini, F.; Egidi, F.; Goings, J.; Peng, B.; Petrone, A.; Henderson, T.; Ranasinghe, D.; Zakrzewski, V. G.; Gao, J.; Rega, N.; Zheng, G.; Liang, W.; Hada, M.; Ehara, M.; Toyota, K.; Fukuda, R.; Hasegawa, J.; Ishida, M.; Nakajima, T.; Honda, Y.; Kitao, O.; Nakai, H.; Vreven, T.; Throssell, K.; Montgomery, J. A., Jr.; Peralta, J. E.; Ogliaro, F.; Bearpark, M. J.; Heyd, J. J.; Brothers, E. N.; Kudin, K. N.; Staroverov, V. N.; Keith, T. A.; Kobayashi, R.; Normand, J.; Raghavachari, K.; Rendell, A. P.; Burant, J. C.; Iyengar, S. S.; Tomasi, J.; Cossi, M.; Millam, J. M.; Klene, M.; Adamo, C.; Cammi, R.; Ochterski, J. W.; Martin, R. L.; Morokuma, K.; Farkas, O.; Foresman, J. B.; Fox, D. J. Gaussian 16, Revision B.01. *Gaussian, Inc., Wallingford CT* **2016**.

(55) Becke, A. D. Density-Functional Exchange-Energy Approximation with Correct Asymptotic Behavior. *Phys. Rev. A* **1988**, *38*, 3098–3100. DOI: 10.1103/PhysRevA.38.3098

(56) Weigend, F.; Ahlrichs, R. Balanced Basis Sets of Split Valence, Triple Zeta Valence and Quadruple Zeta Valence Quality for H to Rn: Design and Assessment of Accuracy. *Phys. Chem. Chem. Phys.* **2005**, *7*, 3297–3305. DOI: 10.1039/b508541a

(57) Francl, M. M.; Pietro, W. J.; Hehre, W. J.; Binkley, J. S.; Gordon, M. S.; DeFrees, D. J.; Pople, J. A. Self-Consistent Molecular Orbital Methods. XXIII. A Polarization-Type Basis Set for Second-Row Elements. *J. Chem. Phys.* **1982**, *77*, 3654–3665. DOI: 10.1063/1.444267

(58) Andrae, D.; Häußermann, U.; Dolg, M.; Stoll, H.; Preuß, H. Energy-Adjusted *ab initio* Pseudopotentials for the Second and Third Row Transition Elements. *Theor. Chim. Acta* **1990**, *77*, 123–141. DOI: 10.1007/BF01114537

(59) Becke, A. D. A New Mixing of Hartree–Fock and Local Density-Functional Theories. *J. Chem. Phys.* **1993**, *98*, 1372–1377. DOI: 10.1063/1.464304

(60) Lee, C.; Yang, W.; Parr, R. G. Development of the Colle-Salvetti Correlation-Energy Formula into a Functional of the Electron Density. *Phys. Rev. B* **1988**, *37*, 785–789. DOI: 10.1103/PhysRevB.37.785

(61) Runge, E.; Gross, E. K. U. Density-Functional Theory for Time-Dependent Systems. *Phys. Rev. Lett.* **1984**, *52*, 997–1000. DOI: 10.1103/PhysRevLett.52.997